corrosion and materials degradation

MDPI

Article

Effect of Heat Treatment on Microstructure and Aqueous Corrosion Properties of AlCoCrNiFe High Entropy Alloy

Soheil Saedi [1], Ahmed Korra [2], Hatim Raji [1] and Hamdy Ibrahim [2,*]

[1] Department of Mechanical and Civil Engineering, College of Engineering and Science, Florida Institute of Technology, Melbourne, FL 32901, USA; ssaedi@fit.edu (S.S.); hraji2022@my.fit.edu (H.R.)
[2] Department of Mechanical Engineering, College of Engineering and Computer Sciences, University of Tennessee, Chattanooga, TN 37403, USA; anasser.korra@gmail.com
* Correspondence: hamdy-ibrahim@utc.edu

Abstract: This study examines the effects of heat treatment on corrosion behavior of equiatomic AlCoCrNiFe high-entropy alloy within a solution treatment temperature range of 800–1100 °C. Experimental observations on phase formation were compared with thermodynamic predictions. The microstructure, mechanical properties, and aqueous corrosion behavior of the as-deposited alloy were analyzed and contrasted with heat-treated samples. The results showed a decline in the corrosion resistance of the AlCoCrNiFe after heat treatment, which was attributed to chemical segregation and Cr depletion in the microstructure matrix. Additionally, post-corrosion analysis revealed a reduced volume fraction of protective oxides in the heat-treated samples.

Keywords: corrosion; high entropy alloys; heat treatment; phase transformation

Citation: Saedi, S.; Korra, A.; Raji, H.; Ibrahim, H. Effect of Heat Treatment on Microstructure and Aqueous Corrosion Properties of AlCoCrNiFe High Entropy Alloy. *Corros. Mater. Degrad.* **2024**, *5*, 561–572. https://doi.org/10.3390/cmd5040025

Academic Editor: Kevin Ogle

Received: 19 July 2024
Revised: 11 October 2024
Accepted: 25 October 2024
Published: 7 November 2024

1. Introduction

High-entropy alloys (HEAs) are novel materials composed of at least four or five equiatomic or near equiatomic principal elements. The multi-component system of HEAs promotes the formation of random solid solutions when specific criteria in terms of alloy design are met [1]. Due to their unique microstructures, HEAs have been reported to show exceptional properties such as high strength, ductility, fatigue life, thermal stability, and corrosion resistance [2]. AlCoCrNiFe is an exemplary HEA, and numerous compositional variants have been extensively explored in recent years. Munitz et al. [3] documented a compressive strength of 2.5 GPa with more than 20% strain for this equimolar composition. The alloy has also displayed remarkably high strength at elevated and cryogenic temperatures [4,5].

In addition to the superior mechanical properties [6], the corrosion resistance of various compositions of AlCoCrNiFe HEAs has been studied in different corrosive environments, such as acidic and alkaline solutions, seawater, and molten salt. Equiatomic AlCoCrNiFe is a single-phase BCC HEA. A complex microstructure comprising multiple phases is formed in the equiatomic alloy when the composition is altered or if the alloy is subjected to heat treatment [7]. Such microstructural variation impacts the corrosion behavior of the alloy drastically. For example, Shi et al. [8] studied the corrosion resistivity of $Al_xCoCrFeNi$ HEA with x = 0.3, 0.5, and 0.7. They reported that Al0.3CoCrFeNi HEA is a single FCC solid solution. However, with the increase in aluminum (Al) content, two BCC-structured (one ordered and one disordered) phases appeared in the microstructure of the Al0.5CoCrFeNi and Al0.7CoCrFeNi HEAs. They also found that the higher Al content resulted in an increased volume fraction of the Cr-depleted BCC phase. The passive film in this phase was less protective than the FCC phase due to a higher quantity of aluminum oxide. This consequently leads to a degradation in resistance to localized corrosion in a 3.5 wt.% NaCl solution. The authors also studied the effect of homogenization on the same compositions, suggesting heat treatment at 1250 °C had a profound influence on

simplifying the microstructure, reducing the elemental segregation, and improving the corrosion resistance [9].

Huang et al. studied the effect of Al addition on the corrosion behavior of $Al_xCoCrFeNi$ HEA (x = 0, 0.1, and 1.0) in supercritical water. They reported that increasing the Al content improves the corrosion resistance in supercritical water [10]. Xie et al. investigated the effect of spark plasma-assisted heat treatment (SPTH) on the corrosion properties of $Al_xCoCrFeNi$ (x = 0.3, 0.7, and 1). In their study, Al0.7CoCrFeNi exhibited the best corrosion resistance after SPTH. They attributed the superior corrosion resistance of this composition, compared to the equimolar variant, to the BCC-FCC transformation in the Al0.7CoCrFeNi.

Meanwhile, the precipitation of the Sigma phase in the equimolar composition was identified as responsible for its lower corrosion resistance [11]. Wang et al. studied the phase, microstructure, mechanical, and corrosion properties of equimolar AlCoCrNiFe prepared by direct laser fabrication in as-deposited and aged at 600 °C, 800 °C, 1000 °C, and 1200 °C for 168 h conditions and compared them to AISI 304L stainless steel [5]. Their evaluation of corrosion resistance was performed using a potentiodynamic polarization (PDP) method in 3.5 wt.% NaCl solution. Their findings indicated a superior corrosion behavior for 304L steel compared to all AlCoCrNiFe HEA samples, regardless of the heat treatment history of the alloy. They also reported an improvement in corrosion resistance after heat treatment at 1200 °C compared to 800 and 1000 °C conditions, which was attributed to the presence of a smaller volume fraction of the FCC phase in the form of larger precipitates. While Al content has been studied more often, Zemanate et al. investigated the effects of Ni concentrations on the microstructure, hardness, and corrosion properties of $AlCrFeCoNi_x$ HEAs (x = 1.0, 1.5, 2.0) [12]. The alloys with higher Ni content displayed a weaker corrosion resistance compared to equimolar alloys. The study also reported degraded corrosion resistance with heat treatment for all studied compositions.

While heat treatment, particularly high-temperature solution treatment, is a common metallurgical practice to refine microstructure and homogenized elemental distribution, such treatment may have a more complex effect on microstructural and elemental homogenization of HEAs than traditional alloys. This is due to HEAs' unique high-entropy effect and diffusion kinetics [13]. The alloy's complex phase transitions and sensitivity to minor variations of treatments may result in inconsistent reports of the alloy's corrosion response. To this end, this study examines the impact of homogenization annealing on phase formation in equimolar AlCoCrNiFe HEA while also evaluating the accuracy of CALPHAD-based predictions for heat treatment. The aqueous corrosion resistance of the alloy heat treated at various temperatures is tested via PDP to correlate the corrosion behavior to the impact of heat treatment on microstructure and phase formations.

2. Materials and Methods

2.1. Samples Preparation

Equiatomic (1:1:1:1:1) AlCoCrNiFe HEA samples were fabricated by ACI Alloys Inc. (San Jose, CA, USA) using the arc casting in inert gas (Argon) method with a diameter of 25.4 mm and a thickness of 3 mm. The material was then cut into 5 mm × 5 mm cubes using an EDM wire cut. Heat treatment was conducted using Lucifer Box Furnace (Warrington, PA, USA). Samples were heat-treated at 800 °C, 900 °C, 1000 °C, and 1100 °C for 10 h. Dry out was made for the furnace before starting the heat-treatment process to ensure a dry condition before purging argon to create an inert environment. The argon-protected environment was ensured by purging argon for more than 30 min at a flow rate between 6–7 CFH and then at a lower flow rate during the heat treatment. The samples were water quenched after heat treatment and labeled.

2.2. Microhardness Test

Microhardness test samples were polished using 180–3000 grit SiC papers in 90° parallel lines to obtain a near mirror surface. The Vickers' hardness of the samples was

measured with a Shimadzu microhardness tester HMV-G Series (Tokyo, Japan) using a 1 kg load cell and 15 s dwell time. Ten measures were taken for each tested sample.

2.3. Potentiodynamic Polarization Test

The PDP test was used to measure the relative change in the corrosion rate due to the heat treatment. A Gamry (Centennial, CO, USA) Instruments Potentiostat was used to perform the test in 3.5 wt.% NaCl solution. Before the test, all the HEA samples (as-received and heat-treated) were polished using 180–3000 grit SiC papers in 90° parallel lines to obtain a near mirror surface. The test was conducted at a voltage varying from −0.3 to 1.00 V relative to the measured OCP at a scan rate of 1 mV/s. In this experiment, we employed conventional three-electrode cells, where the HEA sample was the working electrode, a graphite rod was used as the counter electrode, and a saturated calomel electrode (SCE) served as the reference electrode. Copper wires were used for connections, and the sample surfaces were covered with marine epoxy from all sides except the side that was to be tested for corrosion. The test was conducted at room temperature.

Graphical Tafel analysis using the Gamry Framework was used to obtain corrosion characteristics such as current densities and corrosion potentials. Faraday's law was used to convert the obtained current densities into corrosion rates according to the following equation:

$$CR = 0.00327\ (EW \times I_{corr})/d \quad (1)$$

where CR is the corrosion rate (mm/year), EW is the equivalent weight, I_{corr} is the corrosion current density ($\mu A/cm^2$), and d is the density (g/cm^3). Each coupon's equivalent weight (EW) was calculated according to the following equation.

$$EW = \sum((f_i\ a_i)/n_i) \quad (2)$$

where f_i is the mass fraction, a_i is the atomic weight, and n_i is the valence electrons of each element in the alloy.

2.4. Microstructure Analysis and Characterization

Microstructure characterization was performed using a combination of methods. JEOL JSM-6380LV (JOEL, Tokyo, Japan) scanning electron microscopy (SEM) equipped with energy-dispersive X-ray spectroscopy (EDS) was used to obtain the elements' mappings and chemical compositions. At least three measurements were taken for each EDS spectrum. Microstructural phases were investigated using Empyrean Panalytical X-ray diffractometer (XRD, Malvern Panalytical, Malvern, UK) analysis with Cu Kα radiation with a wavelength of 1.5405 A. The 2θ-scans ranged from 20 to 85°, and a sampling step of 0.05 was used. The Xpert HighScore Plus software Ver. 3.0 was used to analyze XRD peaks. Thermo-Calc® software 2022b and the TCHEA6 database were used to make thermodynamic predictions about phase stabilities, phase compositions, and volume fraction of equilibrium phases as a function of temperature.

3. Results and Discussions

3.1. Microstructure Investigation

Figure 1 shows the SEM-EDS mappings of the alloy in as-received (A.R.) condition. It can be seen that the sample demonstrates a uniform elemental distribution on the surface. EDS analysis in Figure 2 was used to investigate the chemical composition of the area. The EDS spectrum confirms the 1:1:1:1:1 nominal composition of the as-received AlCoCrNiFe HEA.

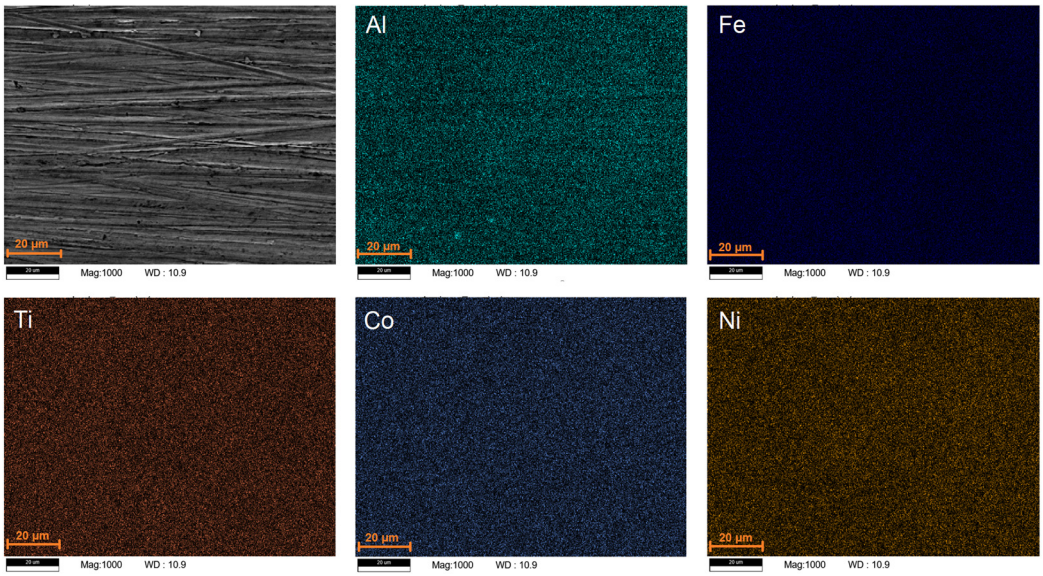

Figure 1. SEM-EDS mappings of the as-received AlCoCrNiFe HEA.

Element	Weight %	Atomic %
Al K	10.86	20.29
Cr K	20.29	19.67
Fe K	22.35	20.18
Co K	23.60	20.19
Ni K	22.90	19.67

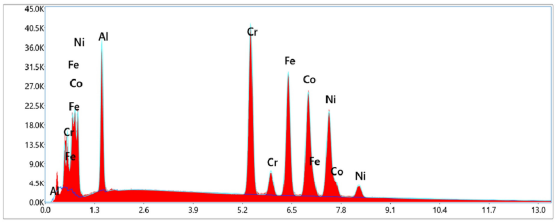

Figure 2. EDS spectrum and measured compositions of the as-received AlCoCrNiFe HEA.

3.2. Thermodynamic Calculations

The equilibrium phase fraction as a function of temperature using the nominal composition is shown in Figure 3. It can be observed that the liquidus temperature for the alloy is approximately 1410 °C. The initially formed solid-phase nuclei at 1405 °C have an ordered BCC-B2 (ORD) structure. It is noteworthy that Thermo-Calc groups BCC and B2 structures as BCC-B2, as the software treats them using the same sublattice. As a result, to differentiate different BCC-B2 phases, an ordering description is used. A secondary disordered BCC-B2 (DISORD) phase is formed with further cooling. FCC appears in a small temperature window of 1100–1000 °C with a tiny volume fraction. The Sigma phase emerges in the temperature range between 1000–600 °C. The volume fraction of the Sigma phase remains almost constant until 660 °C and drops after this point. A single equilibrium simulation was performed at 800 and 1100 °C to analyze the composition of present phases at those temperatures. The results of the single equilibrium calculations are given in Table 1. At 800 °C, the Sigma phase, comprising 30% of the volume, is predominantly rich in Cr (54.9 at%) and Fe (26.6 at%), with no detectable Al and only a trace amount of Ni. As a result, the composition of the BCC-B2 (ORD) phase, which constitutes 70% of the volume fraction, is highly depleted in Cr (5.7 at.%). At 1100 °C, three phases are predicted: BCC-B2 (ORD) at 72.9% volume fraction, BCC-B2 (DISORD) at 27%, and FCC at only 0.1%. Based on compositions presented in Table 1, the BCC-B2 (DISORD) phase in this temperature is highly rich in Cr (45 at.%) and Fe (24.5 at.%) and highly lean on Al and Ni. Hence, the composition of this phase is quite close to the composition of the Sigma phase formed at 800 °C. Similarly, the major part of the volume fraction that belongs to BCC-B2 (ORD) contains a smaller amount of Cr (11.2 at%). At 1100 °C, a tiny fraction of the FCC phase is also observed, again a CrFeCo-rich phase.

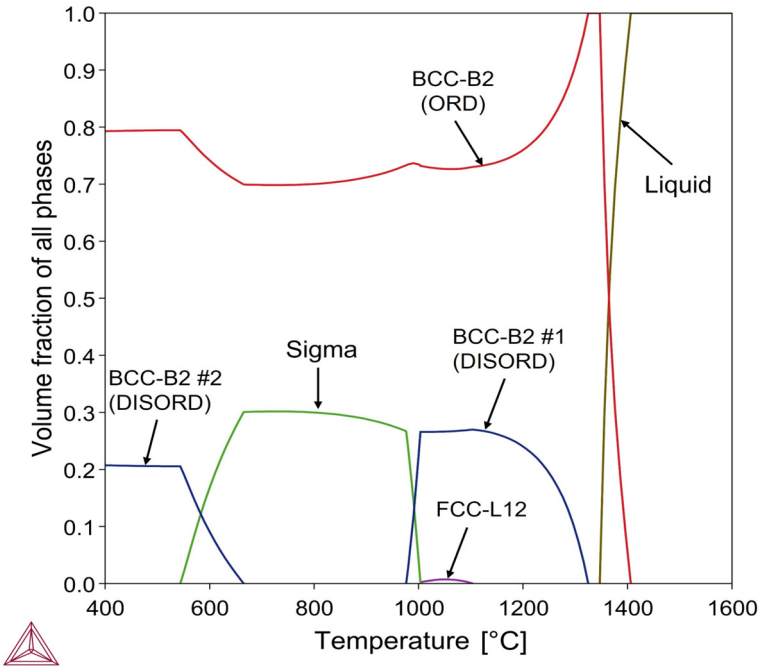

Figure 3. Equilibrium phase diagram calculation for AlCoCrNiFe HEA.

Table 1. Single equilibrium calculations, displaying volume fraction of available phases and their compositions at as-received, 800 °C, and 1100 °C samples.

Sample ID	Phase	Volume Fraction (%)	Composition (at.%)				
			Al	Co	Cr	Ni	Fe
AR	BCC-B2 (ORD)	100	20	20	20	20	20
800 °C	BCC-B2 (ORD)	70	28.2	22.2	5.7	26.7	17.3
	Sigma	30	0.0	14.7	54.9	3.7	26.6
1100 °C	BCC-B2 (ORD)	72.9	25.3	21.2	11.2	24.5	17.7
	BCC-B2 (DISORD)	27	4.9	16.6	44.9	7.1	26.4
	FCC- L12	0.1	5.8	21.7	30.4	14.7	27.4

XRD analysis was performed on the as-received and heat-treated samples, solution-treated at 800 °C and 1100 °C, revealing a significant phase evolution due to heat treatment, see Figure 4. The only present phase in the as-received sample was the BCC phase, matching JCPDS 34–0396. This is consistent with previous studies reporting the dominance of BCC phases in equiatomic AlCoCrNiFe HEAs [14,15]. It can also be seen that heat treatment at 800 °C introduced a significant amount of Sigma (σ) phase to the microstructure to accompany the BCC phase. The Sigma phase was identified and indexed, referring to the Fe–Cr phase (JCPDS 65–4528). The Sigma phase is often known to form at intermediate temperatures, leading to embrittlement and deterioration of mechanical properties in Al-containing HEAs [16]. The XRD results also observed a peak associated with the FCC phase (indexed according to JCPDS 33-0397), which Calphad simulations had not predicted. After heat treatment at 1100 °C, the Sigma phase was absent, and the sample exhibited peaks corresponding to both FCC and BCC phases. The disappearance of the Sigma phase from the microstructure at elevated solution temperatures has been reported before in the literature and was attributed to the stabilization of the FCC and BCC phases with the dissolution of the Sigma phase [17].

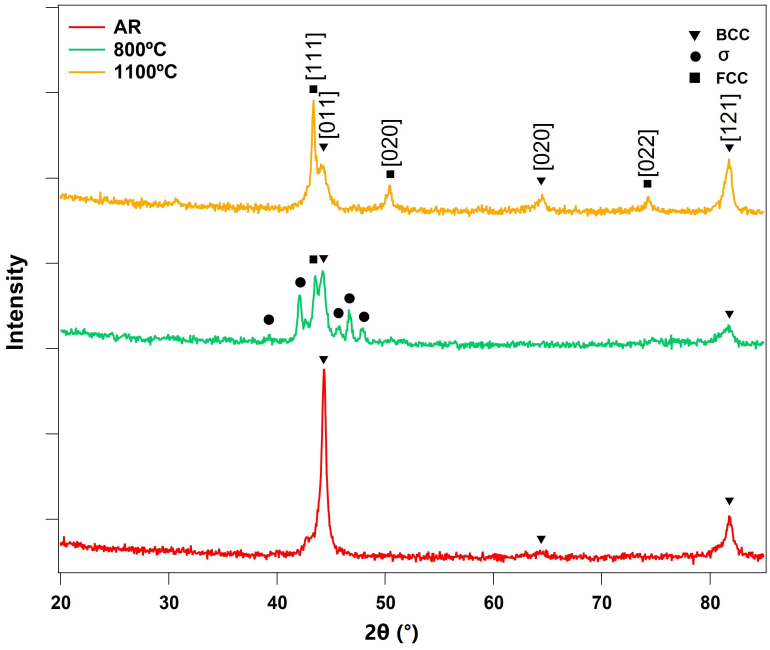

Figure 4. XRD analysis of AlCoCrNiFe HEA in as-received and heat-treated conditions.

3.3. Microhardness

Figure 5 shows the microhardness results of the tested samples to estimate the effect of the heat treatment process on the mechanical properties. The measured microhardness of the as-received sample was 664.5 ± 13.4 HV and dropped to 575.6 ± 9.0 HV after heat treatment at 800 °C. This represents a 13.4% decrease in the microhardness of the alloy after the heat treatment process. By increasing the temperature of the heat treatment to 900 °C, 1000 °C, and 1100 °C, microhardness values continued to decrease further by 26.5%, 32.9%, and 35.4%, respectively, compared to the as-received alloy. These results indicate a significant decrease in alloy hardness after heat treatment. This decrease can be attributed to the formation of the softer FCC phase in the microstructure. The more rigid atomic arrangement of the BCC phase makes it typically harder than the FCC phase, which is generally associated with increased ductility [18]. This effect of the FCC phase formation after heat treatment was also reported by Gali et al. [19]. The microhardness values continue to decline as the volume fraction of the FCC phase increases with heat treatment.

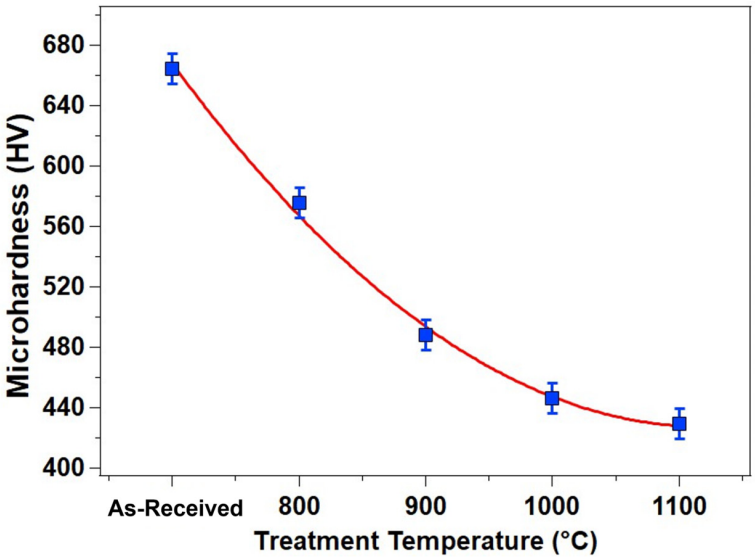

Figure 5. Vickers' microhardness of AlCoCrNiFe as a function of heat treatment temperature.

3.4. Aqueous Corrosion Behavior

Figure 6 shows the PDP Tafel curves of the as-received and heat-treated AlCoCrNiFe HEA groups at 800 °C, 900 °C, 1000 °C, and 1100 °C, and Table 2 lists the corrosion characteristics obtained from these PDP Tafel curves.

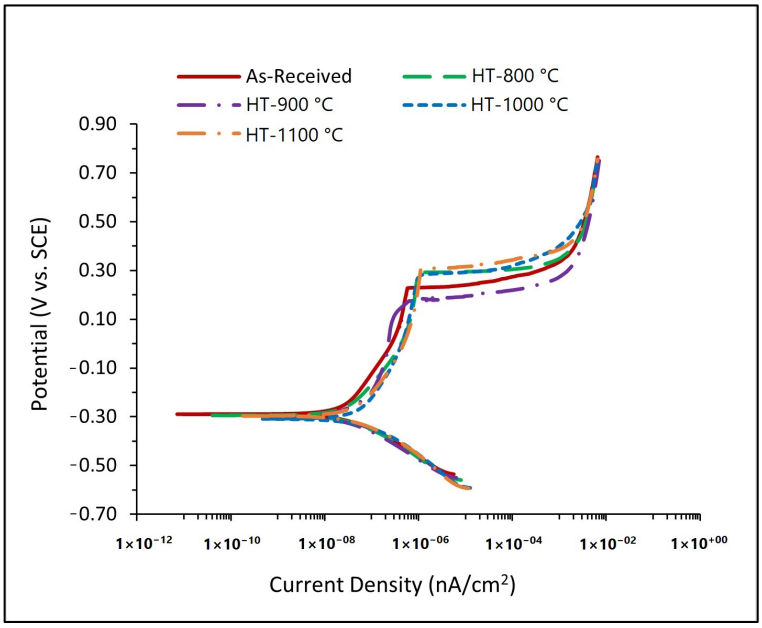

Figure 6. PDP Tafel curves of the equimolar AlCoCrNiFe after various heat treatments.

Table 2. PDP corrosion characteristics of the AlCoCrNiFe HEA groups.

Alloy Sample	I_{corr} (nA/cm^2)	E_{corr} (V)	β Cathode (V/Decade)	β Anode (V/Decade)	CR (µm/Year)
As-received	28.1	−0.289	0.108	0.279	0.275
HT-800 °C	30.5	−0.295	0.236	0.109	0.286
HT-900 °C	49.2	−0.299	0.426	0.119	0.460
HT-1000 °C	61.4	−0.307	0.318	0.122	0.592
HT-1100 °C	62.8	−0.301	0.312	0.132	0.619

The deterioration in the electrochemical corrosion resistance of the heat-treated samples, represented in their higher corrosion current densities compared to the as-received alloy samples, indicates that the alloy became more susceptible to general corrosion in 3.5 wt.% NaCl solution after heat treatment. They also showed an increased negative corrosion potential, as shown in Figure 6, indicating more susceptibility to galvanic corrosion. The details of corrosion characteristics can be seen in Table 2. For instance, the corrosion current density of the as-received sample was 28.1 nA/cm^2, which was increased to 49.2 nA/cm^2 and 61.4 nA/cm^2 when heat-treated at 900 °C and 1000 °C, respectively. The corrosion potential values decreased more negatively from −0.289 V to −0.299 V and −0.307 V when heat-treating at 900 °C and 1000 °C, respectively. This confirms that the heat treatment process resulted in a deterioration in the electrochemical corrosion resistance and led to a higher corrosion rate (C.R.) from 0.275 µm/year for the as-received sample to 0.460 µm/year and 0.592 µm/year for the heat treatment temperatures at 900 °C 1000 °C, respectively.

The microstructural inhomogeneity caused by the introduction of secondary phases in the heat-treated samples has been noted in various studies. Such inhomogeneity leads to galvanic corrosion and more potential for localized corrosion [12,20].

Figure 7 shows the XRD spectra of the as-received, 800 °C, and 1100 °C heat-treated samples after the PDP tests. The XRD patterns detected various oxides after the corrosion process, including Cr_2O_3 (JCPDS 38-1479), Al_2O_3 (JCPDS 46-1212), Co_3O_4 JCPDS (42-1467),

Fe_3O_4, JCPDS (19-0629), and $NiCr_2O_4$ (JCPDS 89-6615). While all samples showed traces of chromium oxide (Cr_2O_3), peaks associated with aluminum oxide (Al_2O_3) were observed in as-received and 800 °C samples. The intensity of the Al_2O_3 peak in the 800 °C sample was slightly higher than that of the as-received. The 800 °C also displayed a peak matched with Co_2O_3, while as-received samples displayed a peak near 30° 2θ, which matched $NiCr_2O_2$ spinel.

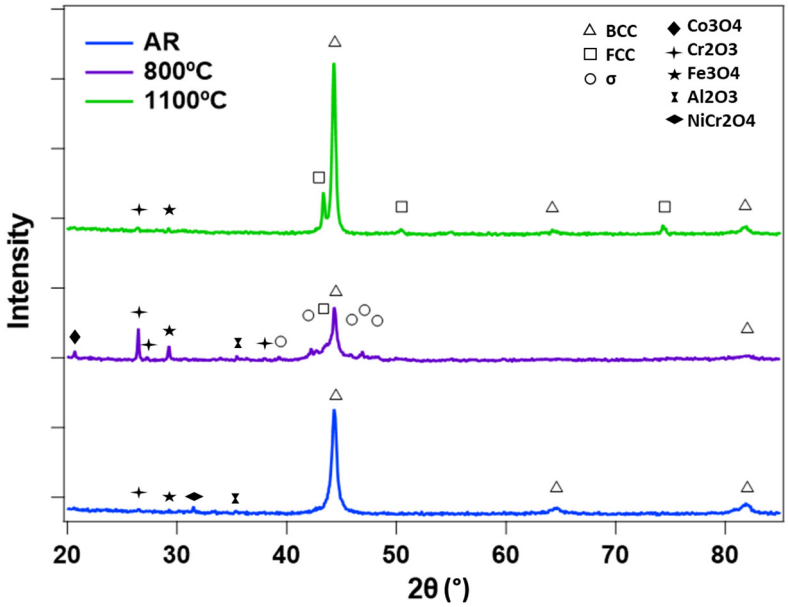

Figure 7. XRD analysis of AlCoCrNiFe HEA in as-received (A.R.) and heat-treated conditions after the PDP test.

Figure 8a–f show the surface morphologies of corrosion pits for the as-received, heat treated at 800 and 1100 °C. In addition, the results of the EDS analysis corresponding to the corroded areas and matrix are presented for each condition. The comparison of the corroded regions revealed that the as-cast samples had the highest oxygen content, whereas the 1100 °C sample exhibited the lowest. The corrosion pit morphology of the as-received sample displayed fine-grained oxides, as seen in Figure 8a,b. The chemical compositions of the corroded regions revealed that the area was predominantly composed of Cr, Fe, and O, designating the constitution of Cr_2O_3 and Fe_2O_3. Although the region is highly depleted in Al and Ni, the EDS analysis of the magnified corroded region showed the darker areas of the corrosion site contained higher Al, designating the constitution of Al_2O_3. Similarly, in the 800 °C sample (Figure 8c,d), the corroded region was dominantly composed of Cr, Fe, and oxygen. EDS analysis of the magnified corrosion site displays two dark and bright phases. Similar to the as-received sample, the darker region was richer in Al than the brighter region. The morphologies of the corroded region of the 1100 °C sample were distinctly different from both as-cast and 800 °C conditions, as can be seen in Figure 8e,f. Rather than refined grains, the corroded region contains two dark and bright regions with distinct boundaries. The overall composition of the corroded region was highly rich in Cr, Fe, and Co, as seen in the table. The oxygen content is considerably lower than in the two other conditions, suggesting the formation of a lower volume fraction of oxides in this sample, which agrees with the XRD results in Figure 7.

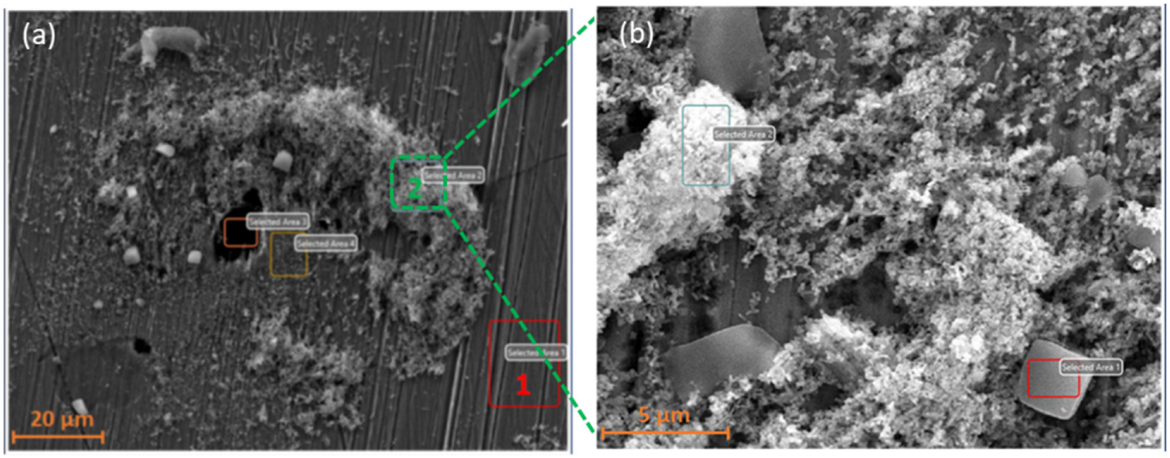

Area	O	Al	Co	Cr	Fe	Ni
1	4.65	19.10	19.27	19.17	19.38	18.42
2	20.17	1.75	13.63	38.86	21.52	4.07

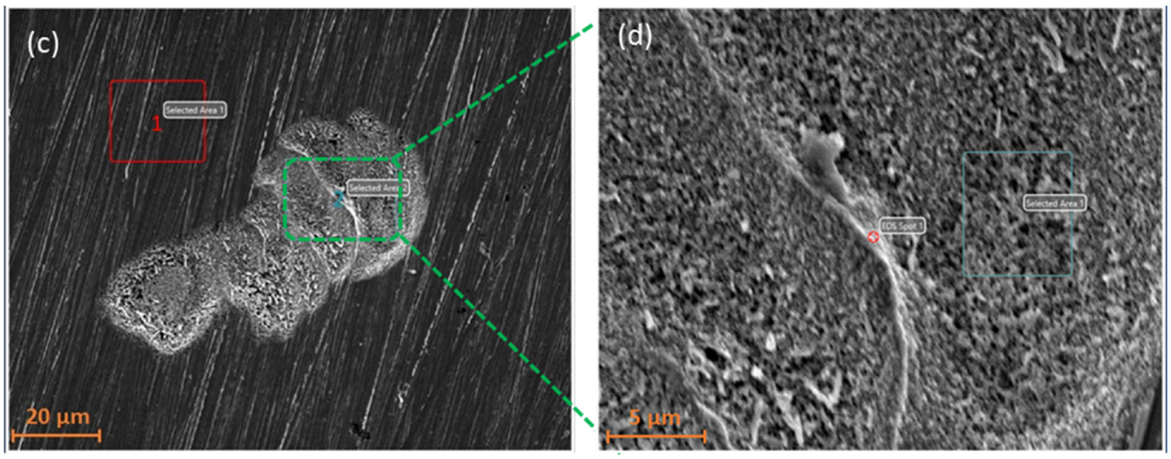

Area	O	Al	Co	Cr	Fe	Ni
1	5.36	24.95	16.30	21.86	11.23	20.30
2	13.27	5.41	16.29	50.55	14.48	

Figure 8. *Cont.*

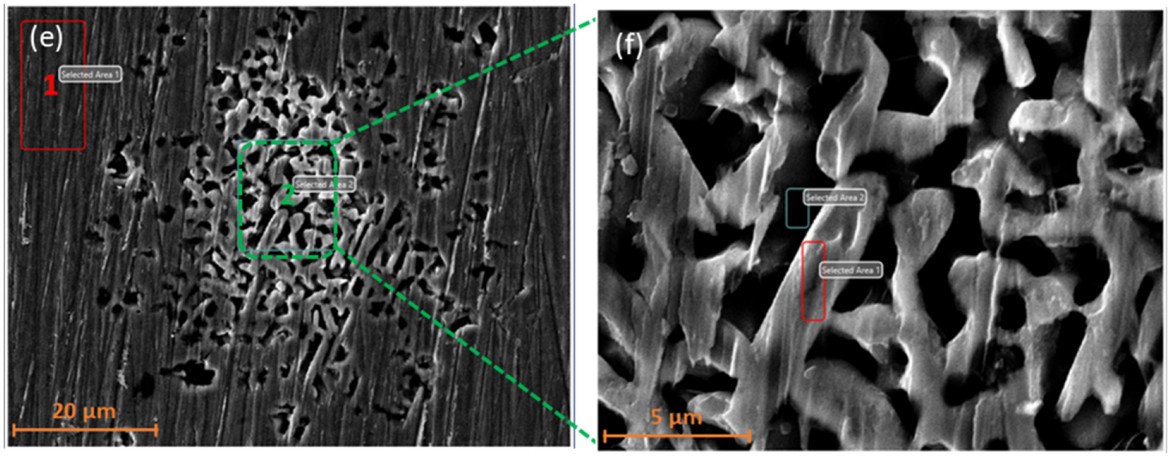

Area	O	Al	Co	Cr	Fe	Ni
1	1.76	11.84	22.05	21.74	22.96	19.65
2	4.87	4.72	21.16	31.61	25.79	11.84

Figure 8. The morphology of corrosion sites and EDS analysis: (**a**,**b**) as-cast, (**c**,**d**) 800 °C, and (**e**,**f**) 1100 °C.

Overall, the superior aqueous corrosion resistance of the as-received condition should be attributed to its single-phase structure. After heat treatment at 800 °C, BCC, Sigma, and a small volume fraction of FCC phases coexist in the microstructure, which the XRD results and phase diagram can validate. The existence of the Cr-Fe-rich Sigma phase in the microstructure is commonly found to be responsible for higher corrosion resistance. The BCC phase in this temperature contains almost 70% of the microstructure, is depleted in Cr, and is rich in Al and Ni, according to Calphad calculations. Given the anti-corrosion effect of Cr, when the Cr-depleted BCC phase dominates the alloy's microstructure, it becomes more prone to aqueous corrosion. The potential difference between the Fe-Cr-rich Sigma phase and the Al-Ni-rich B2 matrix makes the alloy more susceptible to galvanic corrosion, with the B2 matrix preferentially corroding. As a result, a less protective passive layer, which contains a higher amount of Al_2O_3 and a lower amount of Cr_2O_3, is formed on the matrix, evident from EDS analysis showing high Al content in the matrix and depletion of Al in the corrosion pits. These observations and the segregation are consistent with other experimental results obtained using local chemical analysis [6,21–23]. When the heat treatment temperature increases to 1100 °C, the microstructure becomes more complex, and the segregation intensifies to at least three phases: FCC, disordered BCC, and ordered B2 phases. Although the thermodynamic calculations predict a very small volume fraction of the FCC phase, the experimental characterization indicated a notable volume fraction of the FCC phase in this condition. Although the Sigma phase does not appear in this condition, according to the thermodynamic calculations, the composition of the formed disordered BCC phase at this temperature (i.e., 1100 °C) is quite close to the composition of the Sigma phase formed at 800 °C. By forming the third phase FCC, which is again a Cr-Fe-rich phase, Cr is further depleted from the matrix. Furthermore, an increase in microstructural features generally leads to a less homogeneous passive film. This factor can also contribute to the rise in passivation current and reduction in pitting potential. Thus, a combined impact of microstructural complexity and Cr segregation accelerates the corrosion rate for the 1100 °C sample.

4. Conclusions

This study examined the impact of heat treatment on the aqueous corrosion properties of equimolar AlCoCrNiFe high-entropy alloys (HEAs). The as-received material exhibited a single-phase BCC-B2 structure. However, heat treatment at 800 °C led to the formation of a Cr-Fe-rich Sigma phase alongside the BCC phase. At 1100 °C, the Sigma phase disappeared, giving rise to a new Cr-Fe-rich FCC phase and a disordered BCC phase. While the experimental results largely aligned with phase diagram predictions, some discrepancies were observed, particularly in the FCC phase's temperature range and volume fraction. Due to microstructural segregation, the material's microhardness decreased, and its corrosion resistance worsened following heat treatment. Analysis of the corrosion pits revealed the presence of various oxides, most notably chromium and aluminum oxides.

Author Contributions: Conceptualization, S.S. and H.I.; methodology, S.S. and H.I.; software, S.S.; validation, S.S. and H.I.; formal analysis, S.S., A.K., H.R. and H.I.; investigation, S.S., A.K., H.R. and H.I.; resources, S.S. and H.I.; data curation, S.S., A.K., H.R. and H.I.; writing—original draft preparation, S.S., A.K. and H.I.; writing—review and editing, S.S. and H.I.; visualization, S.S. and H.I.; supervision, S.S. and H.I.; project administration, S.S. and H.I.; funding acquisition, S.S. and H.I. All authors have read and agreed to the published version of the manuscript.

Funding: This research received no external funding.

Data Availability Statement: Data is contained within the article.

Conflicts of Interest: The authors declare no conflicts of interest.

References

1. George, E.P.; Raabe, D.; Ritchie, R.O. High-entropy alloys. *Nat. Rev. Mater.* **2019**, *4*, 515–534. [CrossRef]
2. Zhang, Y.; Zuo, T.T.; Tang, Z.; Gao, M.C.; Dahmen, K.A.; Liaw, P.K.; Lu, Z.P. Microstructures and properties of high-entropy alloys. *Prog. Mater. Sci.* **2014**, *61*, 1–93. [CrossRef]
3. Munitz, A.; Salhov, S.; Hayun, S.; Frage, N. Heat treatment impacts the micro-structure and mechanical properties of AlCoCrFeNi high entropy alloy. *J. Alloys Compd.* **2016**, *683*, 221–230. [CrossRef]
4. Qiao, J.W.; Ma, S.; Huang, E.-W.; Chuang, C.; Liaw, P.; Zhang, Y. Microstructural characteristics and mechanical behaviors of AlCoCrFeNi high-entropy alloys at ambient and cryogenic temperatures. In Proceedings of the Materials Science Forum, Columbus, OH, USA, 16–20 October 2011; pp. 419–425.
5. Wang, R.; Zhang, K.; Davies, C.; Wu, X. Evolution of microstructure, mechanical and corrosion properties of AlCoCrFeNi high-entropy alloy prepared by direct laser fabrication. *J. Alloys Compd.* **2017**, *694*, 971–981. [CrossRef]
6. Gao, K.; Liu, D.; Sun, D.; Gao, Y.; Wang, Z.; An, L. Microstructure and properties of AlCoCrNiFe high-entropy alloy sintered by hot oscillating pressing. *Intermetallics* **2023**, *154*, 107802. [CrossRef]
7. Kao, Y.-F.; Chen, T.-J.; Chen, S.-K.; Yeh, J.-W. Microstructure and mechanical property of as-cast,-homogenized, and-deformed AlxCoCrFeNi ($0 \leq x \leq 2$) high-entropy alloys. *J. Alloys Compd.* **2009**, *488*, 57–64. [CrossRef]
8. Shi, Y.; Yang, B.; Xie, X.; Brechtl, J.; Dahmen, K.A.; Liaw, P.K. Corrosion of Al xCoCrFeNi high-entropy alloys: Al-content and potential scan-rate dependent pitting behavior. *Corros. Sci.* **2017**, *119*, 33–45. [CrossRef]
9. Shi, Y.; Collins, L.; Feng, R.; Zhang, C.; Balke, N.; Liaw, P.K.; Yang, B. Homogenization of AlxCoCrFeNi high-entropy alloys with improved corrosion resistance. *Corros. Sci.* **2018**, *133*, 120–131. [CrossRef]
10. Huang, X.; Zhao, Q.; Zhan, Z.; Liu, J.; Liao, X.; Deng, J.; Wei, L.; Li, X. Effect of Al addition on the corrosion behavior of AlxCoCrFeNi high entropy alloys in supercritical water. *Corros. Sci.* **2023**, *216*, 111089. [CrossRef]
11. Xie, S.; Pan, Y.; Fan, Z. Study of the effect of heat treatment on corrosion property of the AlxCoCrFeNi high-entropy alloys (x = 0.3, 0.7, and 1) prepared by spark plasma sintering. *J. Alloys Compd.* **2023**, *968*, 172194. [CrossRef]
12. Zemanate, A.M.; Júnior, A.M.J.; de Lima Andreani, G.F.; Roche, V.; Cardoso, K.R. Corrosion behavior of AlCoCrFeNix high entropy alloys. *Electrochim. Acta* **2023**, *441*, 141844. [CrossRef]
13. Paul, T.R.; Belova, I.V.; Murch, G.E. Analysis of diffusion in high entropy alloys. *Mater. Chem. Phys.* **2018**, *210*, 301–308. [CrossRef]
14. Laplanche, G.; Horst, O.; Otto, F.; Eggeler, G.; George, E. Microstructural evolution of a CoCrFeMnNi high-entropy alloy after swaging and annealing. *J. Alloys Compd.* **2015**, *647*, 548–557. [CrossRef]
15. Miracle, D.B.; Senkov, O.N. A critical review of high entropy alloys and related concepts. *Acta Mater.* **2017**, *122*, 448–511. [CrossRef]
16. Sheng, G.; Liu, C.T. Phase stability in high entropy alloys: Formation of solid-solution phase or amorphous phase. *Prog. Nat. Sci. Mater. Int.* **2011**, *21*, 433–446.
17. Zhou, P.; Xiao, D.; Wu, Z.; Song, M. Microstructure and mechanical properties of AlCoCrFeNi high entropy alloys produced by spark plasma sintering. *Mater. Res. Express* **2019**, *6*, 0865e7. [CrossRef]

18. Wu, Y.-C.; Shao, J.-L. FCC-BCC phase transformation induced simultaneous enhancement of tensile strength and ductility at high strain rate in high-entropy alloy. *Int. J. Plast.* **2023**, *169*, 103730. [CrossRef]
19. Gali, A.; George, E.P. Tensile properties of high-and medium-entropy alloys. *Intermetallics* **2013**, *39*, 74–78. [CrossRef]
20. Izadi, M.; Soltanieh, M.; Alamolhoda, S.; Aghamiri, S.; Mehdizade, M. Microstructural characterization and corrosion behavior of AlxCoCrFeNi high entropy alloys. *Mater. Chem. Phys.* **2021**, *273*, 124937. [CrossRef]
21. Uporov, S.; Bykov, V.; Pryanichnikov, S.; Shubin, A.; Uporova, N. Effect of synthesis route on structure and properties of AlCoCrFeNi high-entropy alloy. *Intermetallics* **2017**, *83*, 1–8. [CrossRef]
22. Garip, Y.; Ergin, N.; Ozdemir, O. Resistance sintering of CoCrFeNiAlx (x = 0.7, 0.85, 1) high entropy alloys: Microstructural characterization, oxidation and corrosion properties. *J. Alloys Compd.* **2021**, *877*, 160180. [CrossRef]
23. Gao, K.; Wu, Z.; Ren, C.; Xiong, Y.; Sun, D.; Gao, Y.; An, L. Microstructures and Properties of AlCoCrNiFe High-Entropy Alloy Sintered by Hot Oscillating Pressing Under Different Sintering Times. *JOM* **2024**, *76*, 2554–2562. [CrossRef]